A Computational Fluid Dynamics Investigation of the 1303 UCAV Configuration with Deployable Rao Vortex Flaps

Michael Atkinson and Frederick Ferguson
Center for Aerospace Research
North Carolina A&T State University
Greensboro, North Carolina, 27411

Abstract

A Computational Fluid Dynamics (CFD) study was conducted on an Unmanned Combat Air Vehicle (UCAV) configuration with deployable Rao Vortex Flaps (RVF). The UCAV configuration of interest to this study is a moderately swept, tail-less, flying wing, that allows for low observability in hostile environments rather than high maneuverability to achieve survivability. The numerical simulations were conducted on a UCAV model that was experimentally tested in two locations; in England using the QinetiQ 5-meter wind tunnel and in the US at NAVAIR. In this analysis, the flaps were modeled as a 0.05-inch thick plate with a deflection angle of 28 degrees relative to the free-stream, and with a height of 5.44% relative to the mean average chord. All CFD computations were conducted using the NASA developed Reynolds Averaged Navier-Stokes flow solver called USM3D. Complementary grid generation software, namely, VGrid and Gridtool, were used to generate the unstructured girds used in the CFD analysis. The USM3D code has both Euler and Navier-Stokes capabilities, as well as, laminar and turbulent capabilities; all of which were deployed in this effort. A major objective of this CFD study was the validation of the UCAV aerodynamics properties; namely, C_D, C_L, C_m, L/D and drag polar, obtained from the wind tunnel experiments reported in previous works. In an effort to, complement the experimental analysis, CFD studies were conducted for angles of attack ranging from 0 to 14 degrees. Results indicated that excellent agreements were achieved between the CFD and experimental analyses. In addition, this study confirmed that the RVP is very effective in reducing drag while increasing the lift over drag performance at higher angles of attack. Results indicated that deploying the vortex flap at angles of attack above 8.5 degrees can potentially reduce C_D and C_m, and increase L/D, thus raising the upper limit of the UCAV's flight envelope.

1.0 - Introduction

The end of the Cold War has brought great changes in the threat to the US national security. Today, the US is much more concerned with a whole host of potential enemies, ranging from terrorists and transnational organizations to rogue nations, whose intentions are highly unpredictable and, therefore, in many ways much more difficult to defend against. To counter this threat, the U.S. military is counting on the acquisition of Unmanned Air Vehicles (UAV's) and other software-intensive weapon systems needed to conduct multiple, concurrent contingency operations worldwide. Within the last few decades, a large number of Unmanned Air Vehicles (UAV's) has been developed for use by the United States military.

Currently, the most popular Unmanned Combat Air Vehicle (UCAV) in use is the General Atomics *Predator*, which has been modified to carry the *Hellfire* missile, refer to Figure 1. It has demonstrated that it is reliability and efficiency in tasks that involve intelligence gathering and real-time battlefield observations. A new-generation of UCAV demonstrators are also being developed by Boeing and Northrop Grumman. However, like the predator, these aircraft are designed for low mission endurance air-to-air and ground-attack roles.

The demands placed on existing systems are numerous; these systems must be flexible and modifiable to perform in any environment. They must be deployable in situations where adversaries do not try to match us plane-for-plane, ship-for-ship, or tank-for-tank. As such, there is a current need for UCAV configurations that incorporates agility and maneuverability. In fact, based on today's requirements, UCAV must have low-observable characteristics and high loitering endurance capability in order to achieve a balanced level of performance. The UCAV configuration of interest to this study is a moderately swept, tail-less, flying wing, that allows for low observability in hostile environments rather than high maneuverability to achieve survivability, Ref. 1-4. An illustration of the UCAV 1303 configuration is illustrated in Figure 2.

Figure 1: Illustration of the Predator UAV

Figure 2: The 1303 UCAV Configuration, Ref 1-4

2.0 - The 1303 UCAV Configuration

Figure 2 illustrates the 1303 UCAV configuration, which was conceived and developed in a joint effort between North Atlantic Treaty Organization (NATO) nations. The 1303 configuration is basically a moderately swept, tailless, flying wing, designed with the goal of being the first stealth UCAV; very much like its predecessor, the B-2 Bomber. The flying wing is extremely well suited for long-duration loitering flights. It is also a configuration that possesses a high degree of stealth by virtue of having little discontinuity in its geometry. However, there are well-known problems associated with the flying wings, which include aerodynamic flutter, low maximum CL and landing gear integration issues. NASA, DoD and NATO have tested a variety of flying-wing-typed UCAV configurations with all experimental results indicating that the 1303 configuration holds the greatest promise. It was concluded in Ref. 1 - 4 that although possessing a number of potential disadvantages, the 1303 flying wing has enough merit to be investigated further as a potential UCAV configuration.

2.1: Theoretical Foundations

The prime aerodynamic characteristic of delta wing-type configurations is the formation of a pair of leading-edge vortices on the upper surface of the wing at angles of attack, Ref 5-6. An illustration of these phenomena is illustrated in Figure 3. The vortices are created by the rolling-up of the shear layer that separates at the leading-edge and is carried downstream by the longitudinal component of the free stream velocity. The rotating flow reattaches to the surface and can separate again to form a secondary vortex. Between the two primary vortices, the flow remains attached to the wing. It is of interest to note that Figure 2 presents a very simplified flow field, and in spite of the numerous studies made on this type of flow, some details of the flow field are not yet very well understood.

The unresolved flow field details can be summed up into to three areas; the transition from laminar to turbulent flow, both on the wing surface and in the rolling shear layer, the presence of vortex breakdown and the nonlinear interaction between vortices.
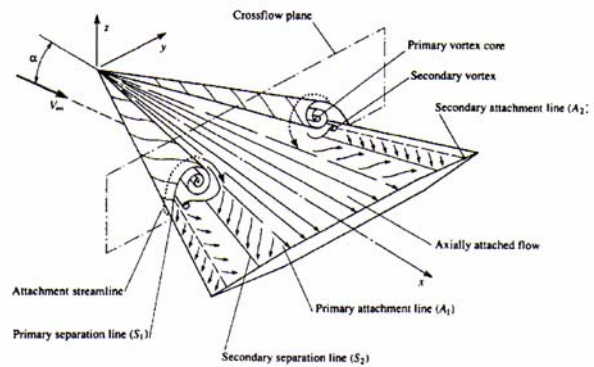
Figure 3: Fowled above a delta wing, Ref 6.

The flow fields around the delta wing-typed configurations are characterized mainly by two vortices that are the sources of energy with very high speeds. The high speed flows in return create a low surface pressure beneath the configurations, producing an additional lift force called the "vortex lift". This lift force increases with increasing angles of attack. Compared to planes with rectangular platforms, this high stalling angle of attack facilitated by the delta wing is a significant advantage when it comes to maneuvering the aircraft.

However, there is a limit to this benefit as the angles of attack get beyond a critical value. The lift does not increase indefinitely with the angle of attack. At large angles of attack the leading edge vortices experience an abrupt change with a sudden expansion of their section, an increase in dynamic pressure and a loss of axial velocity. This phenomenon is called vortex break down or burst. The flow in the breakdown is very chaotic and turbulent although it still maintains a spiral behavior. The position of the breakdown moves upstream with an increasing angle of attack, ultimately

leading to stall conditions; i.e. a region in which the vehicle lift coefficient significantly drops, Ref 5-6.

Although a lot of work has been done to characterize vortex breakdown, no unified theory has emerged to explain the phenomenon. In fact, there are no general agreements when it comes to explaining the difference (if any) between the two types of vortex breakdowns usually observed in experiment. As the phenomenon is not fully understood, the prediction of the position of vortex breakdown relies on experiments and numerical simulations.

Nevertheless, result of experimental investigations indicated that deploying flaps at high angles of attach may delay the vortex breakdown phenomena and thus preserve, and even extend the aerodynamic benefits of the delta-typed wing over a wide range of angles of attack. The CFD study conducted in this analysis seeks validate this concept and further, to analyzed the vortex behavior that was observed experimentally in Ref. 1-4.

2.2: Experimental Observations

Numerous experimental investigations have indicated that deploying flaps at high angles of attach may delay the vortex breakdown over delta-typed wing configurations. Delaying the vortex breakdown phenomena and can preserve the external flow field structure, and even extend the aerodynamic benefits of the delta-typed wing over a wide range of angles of attack. In fact, the CFD study conducted in this analysis seeks validate this concept and further, to analyzed the vortex behavior over the UCAV 1303 configuration that was observed experimentally in Ref. 1-2.

Vehicles with swept wings configurations, such as, the B-2 and the 1303 UCAV, allow for early flow separation and the creation of leading edge vortices at off design conditions, Ref 1. These phenomena can result in high drag penalty and an increase in pitching moment at high angles of attack. However, when controlled, leading edge vortices can produce beneficial effects in the form of increased lift at higher angles of attack and greater maneuverability. Manipulating the leading edge vortices can potentially allow for greater flexibility in vehicle pitch, roll and altitude controls.

It is well known that on vehicles with swept wings, leading edge vortices are created at off-design conditions. The leading edge vortex generally has a beneficial effect in the form of increased lift. By controlling the location of the shed vortex or vortices, vehicle roll and pitch control may be possible. However, UCAV configurations that utilize stealth to avoid detection suffer a radar signature increase when control surfaces are deflected. Thus, there is an advantage to be gained by limiting flap deflection by utilizing vortex flow control to change vehicle attitude. An alternative is to equip the UCAV 1303 configuration with Rao vertex flaps (RVF) to keep the flow attached, thus allowing for better aircraft stability and maneuverability.

At this stage, these behaviors are highly speculative and must be corroborated with experimental and numerical results, Ref. 1-6. In addition, the flow field structures created by the 1303 UCAV configuration with and without RAO flaps are very complex and must be thoroughly studied both numerically and experimentally.

2.3: Experimental Findings

Experimental studies were conducted on the Boeing/US AFRL 1303 UCAV configuration at two locations; namely, at the QinetiQ 5m Tunnel in England, Ref. 4, and at US NATF Facilities at NAVAIR, ref. 3. The computational studies conducted in this effort are directly related to the experimental effort described in Ref. 1-2. Consequently, a brief review of Ref. 1 and 2 efforts is warranted and is provided herein.

Evaluation of the 1303 UCAV was conducted at the NAVAIR Aerodynamic Test Facilities (NATF) in its four-foot by four-foot closed test section, open return wind tunnel. This facility incorporates a 200 horsepower motor that drives a variable pitch fan that delivers a maximum flow velocity of 205 ft/s. In addition, this facility is equipped with honeycomb surfaces and three sets of flow conditioning screens that reduce freestream turbulence intensity to approximately 0.15% and freestream velocity differences to less than 1%. A 4% UCAV configuration with a 47-degree leading edge sweep angle was fabricated from stainless steel. A sting assembly was attached to the model to facilitate testing at angles of attach ranging from zero to 14 degrees. The model was designed and tested with flaps of heights 0.0156 and 0.0417 feet. A model of the deployable serrated flap used in this study is illustrated in Figure 4. It is of interest to note that the single fence DSF used in this study is also referred to as the Rao Vortex Flap (RVF).
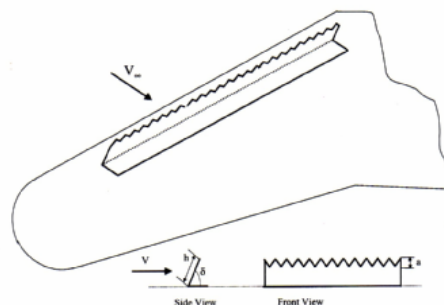
Figure 4: An illustration of the Rao Flap, Ref. 1

The results of this experimental study are discussed in harmony with the CFD solutions obtained from this effort in the latter part of this paper. It is of interest to note that at the time this study was conducted, Dr. James Chung independently confirmed the experimental results through the use of two CFD codes. The codes used were the NASA LARC-developed USM3D code and the commercial off-the-shelf-code Cobalt.
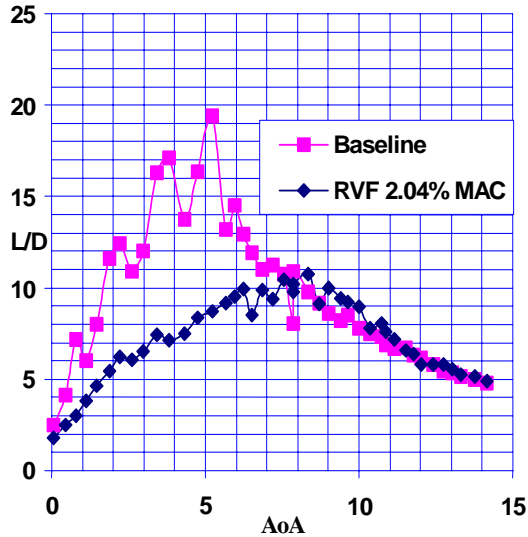
Figure 5: NATF Experiment L/D Findings, Ref 1
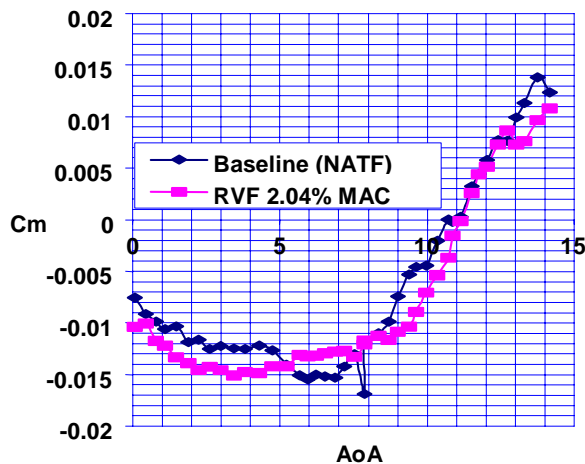
Figure 6: NATF Experiment Cm Findings, Ref 1

The NATF experimental data have shown that at an angle of attack of 8º and above, aerodynamic benefits of the RVF are observed. Improvements in L/D and CM are observed in the experimental plots

illustrated in Figures 5 and 6. In addition, the supporting computational activities conducted Dr. James Chung confirmed these findings. Further insights into these results and their comparison to the computational findings of this effort are discussed later in this paper.

3.0: Computational Analysis

In an effort to directly support the experimental efforts described in the previous section, a Computational Fluid Dynamics (CFD) study was conducted on the 1303 UCAV configuration illustrated in Figure 2. CFD studies were conducted for two cases; a study with RVF and one with out the flaps. The DSF was placed along the leading edge of the of the UCAV starting at 21% of the chord. The fence had a length of 38% of the chord. Numerical simulations were conducted on a 10.8% configuration derived from the UCAV model that was experimentally tested. In this analysis, the RVF was modeled as a 0.05-inch thick plate with a deflection angle of 28 degrees relative to the free-stream, and a height of 5.44% relative to the mean average chord (MAC).

All CFD computations were conducted using a NASA developed Reynolds Averaged Navier-Stokes and Euler flow solver. A series of inviscid and viscous unstructured volume grids with all tetrahedral cells were generated for this study. A major objective of this CFD study, to compare the current results, in terms of C_D, C_L, C_m, L/D, drag polar, with the wind tunnel data obtained in the previous work. A brief description of the CFD tools used in this analysis is provided in the following sections.

3.1: Governing Equations

The fluid motion over the UCAV configuration is governed by the time dependent Navier-Stokes equations. Further, in this analysis, the Navier-Stokes equations are solved with an appropriated numerical representation of the 1303 UCAV configuration along with the corresponding boundary conditions. The solution process is accomplished through the use of the NASA developed TetrSS flowfield solver package. A brief description of this package is presented in the next section.

The Navier-Stokes equations describe the conservation laws with respects to mass, momentum and energy for a compressible ideal Newtonian fluid in the absence of external forces. In this analysis and as illustrated in Ref. 7, the Navier-Stokes equations are implemented in the integral form over the domain, Ω, which is enclosed by the boundary, $\partial\Omega$:

$$\frac{\partial}{\partial t}\iiint_\Omega QdV + \oiint_{\partial\Omega} F(Q)\cdot\hat{n}dS = \oiint_{\partial\Omega} G(Q)\cdot\hat{n}dS$$

where the vectors; Q, F and G are defined as follows:

$$Q = \begin{Bmatrix} \rho \\ \rho u \\ \rho v \\ \rho w \\ e_o \end{Bmatrix}$$

and

$$F(Q) \cdot \hat{n} = \left(\hat{V} \cdot \hat{n}\right) \begin{Bmatrix} \rho \\ \rho u \\ \rho v \\ \rho w \\ e_o + p \end{Bmatrix} + p \begin{Bmatrix} \rho \\ \hat{n}_x \\ \hat{n}_y \\ \hat{n}_z \\ 0 \end{Bmatrix}$$

and

$$G(Q) \cdot \hat{n} = \frac{M_\infty}{Re_L}\left(\hat{n}_x G_1 + \hat{n}_y G_2 + \hat{n}_z G_3\right)$$

The expressions for the G_i, $i = 1, 3$, are listed as follows:

$$G_1 = \begin{Bmatrix} 0 \\ \tau_{xx} \\ \tau_{xx} \\ \tau_{xx} \\ u\tau_{xx} + v\tau_{xx} + w\tau_{xz} - \dot{q}_x \end{Bmatrix}$$

$$G_2 = \begin{Bmatrix} 0 \\ \tau_{xy} \\ \tau_{yy} \\ \tau_{xz} \\ u\tau_{xy} + v\tau_{yy} + w\tau_{yz} - \dot{q}_y \end{Bmatrix}$$

and

$$G_3 = \begin{Bmatrix} 0 \\ \tau_{xz} \\ \tau_{yz} \\ \tau_{zz} \\ u\tau_{xz} + v\tau_{yz} + w\tau_{zz} - \dot{q}_z \end{Bmatrix}$$

Similarly, expressions for the shear forces in the x, y and z directions acting on the appropriate elementary surfaces, $\tau_{xx}, \tau_{yy}, \tau_{zz}, \tau_{xy}, \tau_{yz}$ and τ_{zz} are listed as follows:

$$\tau_{xx} = 2\mu u_x - \frac{2}{3}\mu\left(u_x + v_y + w_z\right)$$

$$\tau_{yy} = 2\mu v_y - \frac{2}{3}\mu\left(u_x + v_y + w_z\right)$$

$$\tau_{zz} = 2\mu w_z - \frac{2}{3}\mu\left(u_x + v_y + w_z\right)$$

$$\tau_{xy} = \mu\left(u_y + v_x\right)$$
$$\tau_{xz} = \mu\left(u_z + w_x\right)$$
$$\tau_{yz} = \mu\left(v_z + w_y\right)$$

The expressions describing the heat conduction rates are as follows:

$$\dot{q}_x = -\frac{\mu}{Pr(\gamma-1)}\frac{\partial T}{\partial x}$$

$$\dot{q}_y = -\frac{\mu}{Pr(\gamma-1)}\frac{\partial T}{\partial y}$$

$$\dot{q}_z = -\frac{\mu}{Pr(\gamma-1)}\frac{\partial T}{\partial z}$$

The equations are nondimensionalized with free-stream reference values for density, ρ_∞, and the speed of sound, a_∞. In this analysis, the normal vector to the exterior surface, $\hat{n}$, has the following components, $\hat{n}_x$, $\hat{n}_y$, and $\hat{n}_z$, in the *x, y* and *z* directions, respectively. The term e_o represents the total energy per unit volume of the fluid. The Prandtl number, Pr, is assigned a value of 0.72. Viscosity is computed by Sutherland's law. When the ideal gas assumption is used the normalized values for pressure and temperature can be expressed as follows:

$$p = (\gamma-1)\left(e_o - \frac{1}{2}\rho\left(u^2 + v^2 + w^2\right)\right)$$

and

$$T = \gamma\, p/\rho$$

where γ is the ratio of specific heats and is prescribed as 1.4 for air.

4.0: NASA TetrUSS Flow Solver

USM3D is an efficient Navier-Stokes equation solver for unstructured tetrahedral cells developed by NASA Langley Research Center (LARC), Ref. 8-18. In fact, the USM3D code is an important part of the NASA Tetrahedral Unstructured Software System (TetrUSS). The flow field routine solves the spatial discretization flowfield domain by a cell-centered, finite volume formulation using Roe's flux difference splitting for

upwinding. A novel cell reconstruction process, based on an analytical formulation for computing solution gradients within tetrahedral cells, is used for the higher order differencing. Solutions are advanced in time by a three-stage Runge-Kutta time stepping scheme with convergence accelerated to steady state by local time stepping and implicit residual smoothing. Refinements to the data structure of the code have resulted in reduced memory requirements and increased speed.

The primary attractiveness of tetrahedral-based schemes hinges on the demonstrated capability of rapid grid generation over a wide range of complex geometries by a variety of users. Gridtool and Vgrid are two complementary codes, which are part of the TetrUSS family, that are widely used in harmony to rapidly generate inviscid and viscous tetrahedral grids over aircraft configurations. The Vigplot code on the other hand, complements the TetrUSS family of CFD codes by providing the much needed visualization capabilities.

4.1:   UCAV 1303 Configuration

The numerical models used in this study were derived from the configuration UCAV configuration that was tested with RVF flaps at NAVAIR, refer to Figure 2. The numerical representation of the deployable serrated flap used in this study was derived from the model illustrated in Figure 4. In addition, all numerical models used in this investigation were constructed with an appropriate geometric representation of the sting that was attached to the experimental model. A Computer Aided Design (CAD) representation of the UCAV 1303 model is illustrated in Figure 5.
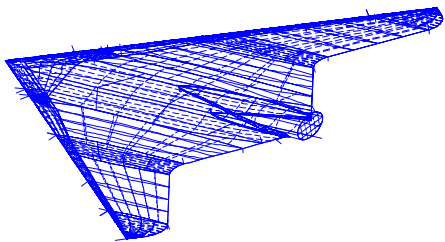
Figure 7: A CAD illustration of NATF 1303 UCAV

4.2:   VGrid and GridTool

VGrid is a graphical user friendly, interactive visualization tool that bridges the gap between the CAD derived numerical model (illustrated in Figure 5) and the grid generation tools required for effective CFD analysis (illustrated in Figure 6), Ref. 9-12. The baseline 1303 CAD configuration used in this CFD analysis was provided by NAVAIR. However, the geometry was modified slightly through the use of Gridtool, with the objectives of accommodating

appropriate geometric requirements for the RVF flaps and the sting. The sting was mounted to the rear of the UCAV model in an effort to better reproduce the wind tunnel testing conditions. In addition, Gridtool is used iteratively through out this study to facilitate the generation of grids need for USM3D flow field simulations.

Two sets of numerical models were developed; a set of two models with flaps and a second set of two models without flaps. In addition, within each set of numerical models two sets of grids were developed; namely, an inviscid grid was constructed around the first model and a viscous grid around the second. As such, a total of four computational models were created for the USM3D analysis. All tasks, such as, surface triangulation, the generation of inviscid and viscous volume grids, and the grid refined of existing grids are conducted through the use of Vgrid and Postgrid.

It is of interest to note that Vgrid generates unstructured tetrahedral finite volume grids based upon the advancing front advancing layers method, Ref. 8-9, which is very reliable and accurate. On the other hand, Postgrid is equipped with the addition capability of smartly closing any remaining holes within the flow domain.
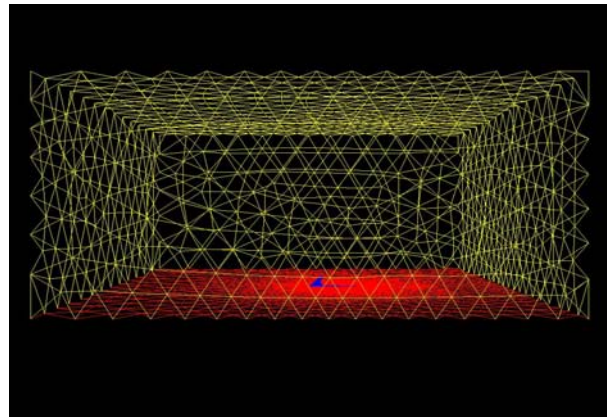
Figure 8: Illustration of the UCAV Flow domain
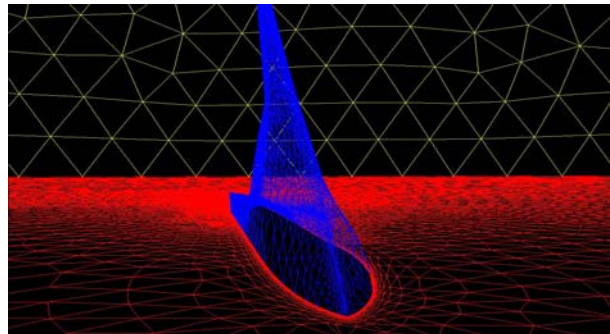
Figure 9: A Close-up Illustration of UCAV Grids

4.3: Boundary Conditions

Prior to any CFD analysis, the user must specify the surface, near and far field boundary conditions. In addition to the respective boundary conditions, the grid sources, sizes, location, spacing and strength must be computed. This process is automated within Gridtool routines. Typical representations of the UCAV with its computational grids prior to USM3D evaluation are illustrated in Figures 6 and 7.

As part of the USM3D code the pseudo-Laplacian averaging method is applied to the boundary nodes. The implementation of this process required the implementation of ghost cells. Ghost cells are produced by constructing an image cell across the exterior boundary of an adjacent interior cell. The geometric information is supplied by vector relations

$$x_{gh} = \left(x_{c,i} - x_{n_b}\right) - 2Xn_x$$
$$y_{gh} = \left(y_{c,i} - y_{n_b}\right) - 2Xn_y$$
$$z_{gh} = \left(z_{c,i} - z_{n_b}\right) - 2Xn_z$$

where

$$X = \left(x_{c,i} - x_{n_b}\right)n_x + \left(y_{c,i} - y_{n_b}\right)n_y + \left(z_{c,i} - z_{n_b}\right)n_z$$

is a contravariant vector component of distance, and the subscript n_b denotes the a boundary node. These coordinates are used only in the initial generation and storing of the weighting factors and are not used there after.

The flow information within the ghost cells must be updated throughout the solution process. For solid boundaries, the flow tangency condition is imposed at the nodes by constructing an image of the interior velocity vector within the adjacent ghost cell. As before, this is accomplished by subtracting twice the contravariant velocity from the adjacent interior cell velocity vector:

$$u_{gh} = u_{c,i} - 2Un_x$$
$$v_{gh} = v_{c,i} - 2Un_y$$
$$w_{gh} = w_{c,i} - 2Un_z$$

where

$$U = u_{c,i}n_x + v_{c,i}n_y + w_{c,i}n_z$$

For viscous, no-slip boundaries, negative values of the cell-centered velocity components are assigned to the corresponding ghost cell. The density and pressure within the ghost cell are set equal to the values in the adjacent interior cell.

Flow tangency is enforced on solid inviscid boundary faces by subtracting the contravariant velocity component normal to the surface. A condition of zero mass and energy flux through the surface is ensured by setting the left and right states of solid boundary faces equal to the boundary conditions prior to computing the fluxes with Roe's approximate Riemann solver. This technique only permits a flux of the pressure terms of the momentum equations through a solid boundary.

The viscous, no-slip boundary conditions take advantage of the inherent "structure" in the grid imposed by the Advancing-Layers Method (ALM) of Ref. 8-9. The ALM produces thin-layer tetrahedral grids with nodes in the "viscous region" distributed along predetermined surface vectors. Thus, as for structured grids, the pres sure can be extrapolated to the boundary nodes by a two-point formula. Density is determined by either an adiabatic condition or a prescribed temperature, and velocity at the nodes is explicitly set to zero. Once the nodal quantities are set on the boundary the face boundary conditions for pressure and density are determined. The velocity is explicitly set to zero on the boundary faces.

Characteristic boundary conditions are applied to the far-field subsonic boundary using the fixed and extrapolated Riemann invariants corresponding to the in coming and outgoing waves. The incoming Riemann invariant is determined from the freestream flow and the outgoing invariant is extrapolated from the interior domain. The invariants are used to determine the locally normal velocity component and speed of sound. At an outflow boundary, the two tangential velocity components and the entropy are extrapolated from the interior, while at an inflow boundary they are specified as having far-field values.

5.0: Flow Solver USM3D

The flow fields around the UCAV configuration of interest to this project were computed with an efficient equation solver for unstructured tetrahedral cells, Ref. 13 - 18. In this method, the spatial discretization is accomplished by a cell-centered finite-volume formulation using Roe's flux-difference splitting. A novel cell reconstruction process, which is based on an analytical formulation for computing solution gradients within tetrahedral cells, is used for the higher-order differencing. Solutions are advanced in time by a 3-stage Runge-Kutta time-stepping scheme with convergence accelerated to steady state by local time stepping and implicit residual smoothing. Recent refinements to the data structure of the code have resulted in an improved efficiency for the flow solver.

The resulting version of the code has increased the speed from about 20.5 milli-sec/cell/iteration to 17.5 milli-sec/cell/iteration on a CRAY-YMP, and has decreased the required memory from 64 words/cell to about 45 words/cell. For tile present calculations this translated to between 19.5 and 31.6 mega words of core memory.

Tetrahedral viscous and inviscid grids were generated over the UCAV 1303 configuration illustrated in Figure 5. The viscous grid over the UCAV model

with the Rao flaps, shown in figures 6 and 7, has over 2,933,106 cells and the model without flaps contained 748,296 calls. The grids used in this analysis were generated using a SGI Indigo workstation with a R4000 (100MHZ) processor.

For all computations, the outer boundaries were located at 6 root chord lengths (6C) ahead, above and below the UCAV configuration. In the spanwise direction, the outer boundary was 2.5C away from the symmetry plane. For all tile cases, a 29 x 23 x 7 background grid was used. The grid spacings were specified using 8 "point" and 13 "line" sources. The line source positioned along the axis of tile store propagates symmetrically, while the line sources along the leading and trailing edges of the UCAV have directional intensity control. The eight point sources were placed at tile corners of the outer computational boundaries. A single surface mesh was generated and maintained for all subsequent volume grids. The surface triangulation, shown in Figure 7, consists of 13,526 points and 27,044 triangles including the grid on the plane of symmetry and outer computational boundaries.

5.1:   Time Integration

The computations are advanced to steady state by the implicit time advancement strategy of Anderson et al, Ref. 10-11. The scheme uses the linearized, backward Euler time differencing approach to update the solution at each time step. The linear system of equations are solved at each time step with a point-Jacobi subiteration on groups of tetrahedral cells which are separated into 'colors' (different from face-coloring) such that no two cells share a common face. While the point-Jacobi method is in itself not very efficient, convergence rate is accelerated by using the latest values of the updated solution variables as soon as they are available after subiteration of prior 'colors'. This produces a Gauss-Seidel-like effect, and the method has the advantage of being completely vectorizable. Typically, 10 subiterations are used for Navier-Stokes computations and 20 subiterations for Euler.

5.2:   Turbulence Model

The Spalart-Allmaras turbulence model was selected as part on this numerical investigation, Ref. 18. Closure of the Reynolds stress is provided by the one-equation Spalart-Allmaras (S-A) turbulence model, Ref. 18. This model is derived "using empiricism and arguments of dimensional analysis, Galilean invariance, and selective dependence on the molecular viscosity". The model solves a partial differential equation (PDE) over the entire field for a transformed working variable from which the eddy viscosity can be extracted. The PDE is solved separately from the flow equations using the same back ward Euler time integration scheme, which results in a loosely coupled system. The production and destruction terms have been modified as recommended in Ref. 18 to ensure positive eddy viscosity throughout the computation.

On 'no-slip' surfaces, the dependent variable, 'v', is set to zero. For tangent-flow surfaces, a zero gradient of the variable is applied. Far field boundary conditions are applied by extrapolating from the interior for outflow boundaries, and taken from the free stream for the inflow. The S-A model requires that the distance of each cell to the nearest wall be provided for the near-wall damping terms for cells which are in proximity to 'viscous' surfaces. These distances are determined prior to code execution for cells in the "viscous" layers.

It is of interest to note that within the USM3D code, the S-A model has been coupled with a wall function formulation to eliminate the need for resolving the flow in the sublayer portion of a turbulent boundary layer. Details of this approach are presented in Ref. 16. With this approach, the inner region of the boundary layer is modeled by an analytical function which is matched with the numerical solution in the outer region. This has the advantage of 1) significantly reducing memory requirement by eliminating a large portion of cells normally required to resolve the sub- layer, and 2) improving overall convergence by removing the thinner, more highly stretched cells which add stiffness to the solution process. In USM3D, the selected wall function is a law-of-the-wall expression derived by Spalding in 1961. However, the present implementation (for low Mach numbers) considers no adjustment to adiabatic wall density, which becomes very important for high speed flows.

6.0:   Computational Results

This section presents the CFD results obtained for all the numerical models described earlier. Since the primary aim of this paper is to validate the experimental results of the UCAV 1303 investigation conducted in Ref. 1-4, for the most part the results are presented in the form of aerodynamic performance plots; namely, C_D, C_L, C_m, L/D and drag polar versus the angle of attack, (AOA). Some surface contour plots in the form of Oil flow visualization are also presented.

6.1:   Computational Models

A total of four numerical models were created and tested under similar freestream conditions. Two inviscid models were created, one with the RVF and one without. The model with the RVF contained a total of 748,296 cells and, the model without the RVF contained 460,842 cells. Similarly, two viscous models were created, one with the RVF and one without. The model with the RVF contained a total of 2,933,106 cells and, the model without the RVF contained 748,296 cells.

All models were of 10.8% half-configurations. They were tested at a sub-sonic Mach number, M, of 0.17 and at a Reynolds's number, Re, of 4.3 million/ft. Test runs were conducted under varying angle of attacks, ranging from 0 to +14 degrees. All computations were conducted using the Spalart-Allmaras one-equation turbulence model, Ref. 18. Each half-configuration model, inviscid and viscous, has a reference area (S), of 466.67in², reference span (b), 30.002in, aspect ratio of 3.857, and mean average chord (MAC) 21.25in, with moment references of 18.065in, 0.000in, and 8.355in, in the *x, y, z* direction, respectively.

The RVF models had a slight change in references quantities. Obviously, there was a slight increase in the total surface area of the model due to the introduction of the RVF. The RVF spanwise location was 21% y/b, and length of 38% y/b. The RVF chordwise location is 1.25% MAC, has height of 5.44% MAC, with a thickness, t, of 0.05in. with a deflection angle, δ, of 28º, relative to the freestream. The CFD models used the same design parameters as the NAFT experimental conditions, with exception of the height of the RVF. The experiment models were developed with a RVF height of 1.25% of the MAC, where as, the CFD model used a RVF height of 2.04% MAC. The increase in the height of the CFD models was necessary for the creation of an appropriate computational grid.
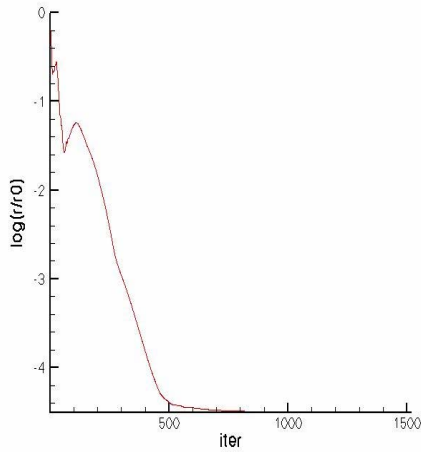
Figure 10: Flow field Convergence studies

6.2: Solution Validation

An average of 3000 iterations was need for convergence, based on the performance parameters of interest to this investigation. The aerodynamic parameters of interests were CL, CD, and CM. It was observed that the convergence rate was dependent on the angle of attack. A maximum of 12225 iterations was

need for convergence at an angle of attack of 14º in the case of viscous grids. A typical convergence plot obtained from this study is illustrated in Figure 10. Once convergence is attained, formatted data for C_L, C_D, C_M, and C_P are generated and analyzed.

7.0:   Computational and Experimental Results
7.1: Baseline Configuration Studies

In this report, the baseline model is referred to as the numerical model without RVF. And, as described earlier, the baseline models were simulated under viscous and inviscid conditions. In particular, CFD results of the 10.8% baseline models were compared to the results obtained from the 5-meter wind tunnel Qinetiq tests, Ref. 4, and the data were used to serve as the validation exercise of this investigation. The results of this effort are presented in Figures 12 and 13.
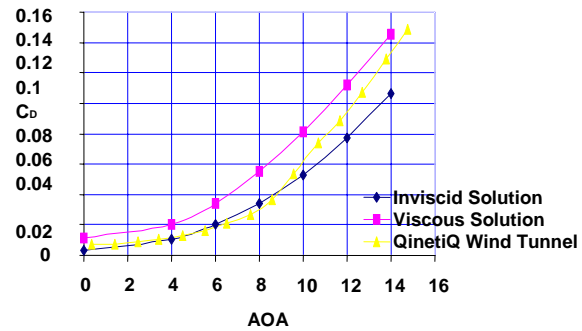
Figure 11: C_D Numerical and Experimental results
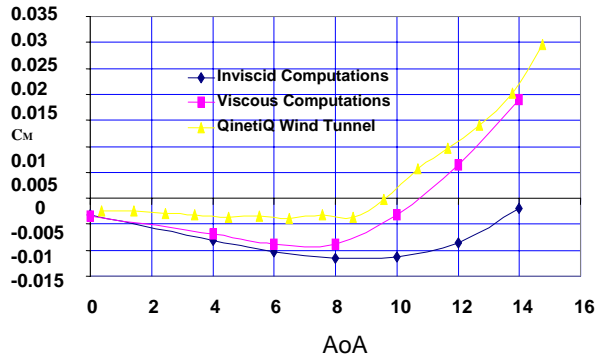
Figure 12: C_M Numerical and Experimental results

Figures 11 and 12 data have yielded interesting results, when comparing the computational and

experimental data. As noted, the inviscid volume grids were created in order to generate preliminary results quickly. However, the data seems to indicate that the experimental results seem to lie some where in the middle of the inviscid and viscous computations. It is of interest to note, that the inviscid models exactly predicted C_D as a function of the angle of attack, for α ranging form 0° to 8°, while the viscous solution yielded a difference of approximately 1% from the experimental data. Overall, the viscous solution yielded better results for C_M, C_D, and L/D, when compared to the experimental data.

A closer look at these results reveals an interesting insight to the flow structure and may even impact the choice of the turbulence models used in future studies. The assumption of fully turbulent flow may not be the case for the 1303 UCAV configuration at AoA below 8°. The flow may still be attached or even laminar at low AoA. This conclusion is supported by the oil flow data illustrated in Figures 13. Similar results were also obtained from the Qinet data, as illustrated in Figures 14 and 15.
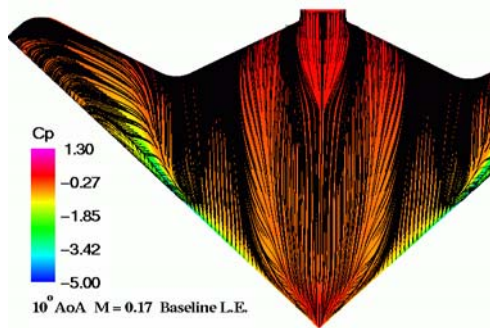
Figure 13: Oil Flow baseline AoA 10°
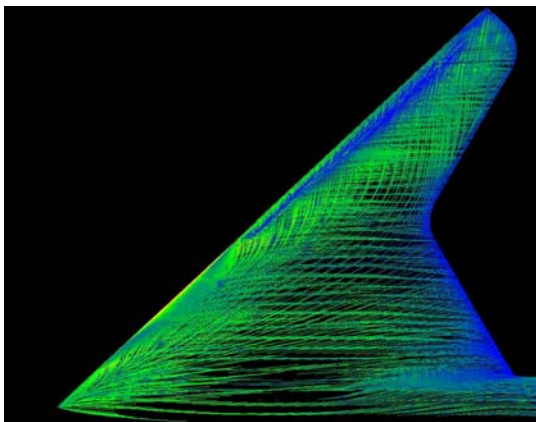
Figure 14: Oil Flow baseline AoA 8°, Ref. 4

Figures 12 and 13 highlight the oil flow pattern solutions for angles of attach of 10 and 14 degrees. These results are very typical of the expected flow fields over the UCAV configuration since they exemplify the physic behaviors of the expected flow fields. In addition, by highlighting the pressure coefficient on the flow pattern designers may begin to gain new insights about the behavior of the flow field around the 1303 UCAV configuration.
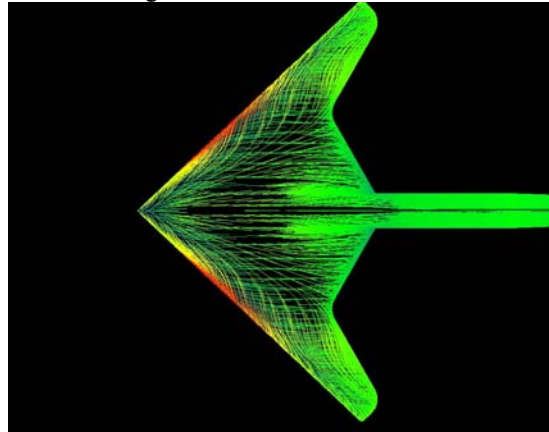
Figure 15: Oil Flow baseline AoA 12°, Ref. 4

7.2: Results of UCAV with RVF

A major objective of this investigation is the confirmation of the NAVAIR experimental results that indicated that the deployable RVF offers significant aerodynamic benefits at high angles of attack. The CFD results presented in Figures 16, 17 and 18 validated the experimental findings obtained in Ref. 1-4. In fact, it is shown that at an angle of attack of 8° the RVF reduces the drag and provides the vehicle with a 6% increase in L/D. Results also showed that the pitching moment increases by 4% at an angle of attack of 8°. These results were compared to the baseline configuration under similar free stream conditions.
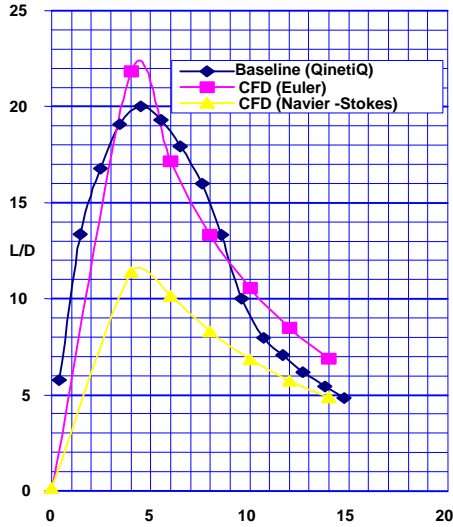
Figure 16: L/D Numerical and Experimental results
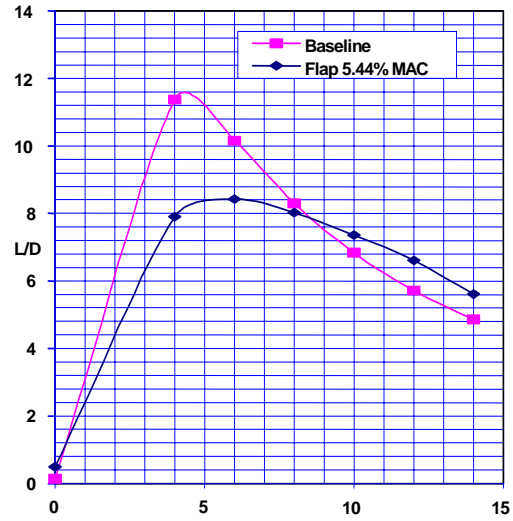
Figure 18: L/D baseline and RVF viscous models

8.0: Concluding Remarks

A brief description of the CFD solution over a 1303 UCAV configuration was presented. In addition, brief descriptions of the TetruSS software system, its algorithmic features, the capabilities of the tetrahedral-based finite-volume Euler and Navier-Stokes flow solver USM3D and complementary grid generation codes were documented. This code, along with the tetrahedral grid generator, VGRID, is primary components of the NASA TetrUSS package which is being used extensively throughout the U.S. for solving complex aerodynamic problems. The Navier-Stokes capability is maturing rapidly as a result of many focused customer applications on a range of configurations. The present work has addressed its easy of use, its accuracy and robustness.

Excellent prediction of force-moments and surface pressures on the 1303 UCAV configuration was achieved with as few as 1.2 million tetrahedral cells, and within 2 wallclock per solution on a CRAY C90. While many more application studies are needed to increase user confidence in this capability, these results serve to demonstrate the strong potential for tetrahedral-based finite-volume Navier-Stokes methodologies to become a practical computational aerodynamic tool.

The results of this investigation have confirmed the aerodynamic benefits of a deployable RVF on the upper surface of flying wing UCAV configuration. The CFD results predicted that in the neighborhood of 8º angle of attach the deployable RVF can generate more lift than a vehicle without a RVF. By reducing drag and decreasing the slope of the pitching moment a more aerodynamically stable vehicle can be built.

This study, however, still leaves the nature of the flowfield around the 1303 UCAV configuration questionable. The preliminary data seems to attribute the increase in L/D at higher angles of attack to the increase in the center of pressure along the wing. The flap causes laminar flow under the spanwise direction of the RVF, from the wing apex and leading edge thus the more flow remained attached to the wing, which would otherwise form into apex vortices. This suction also reduced the strength of the leading edge vortices and strengthens the laminar suctioned flow. Anyway, since a fully turbulent S-A turbulent model was the only one implement in this study this conclusion may be questionable and may serve as the basis for future work.
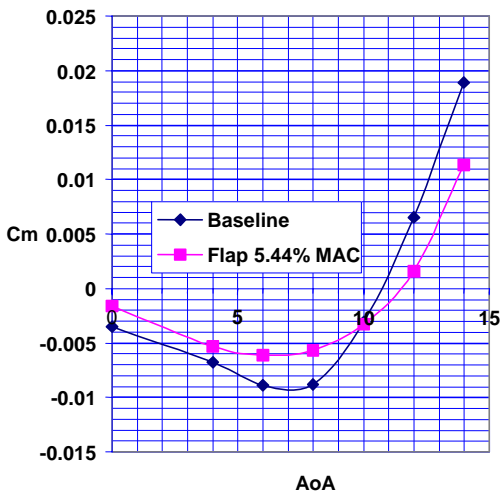
Figure 17: CM baseline and RVF viscous models

9.0: Acknowledgements

10: References

1. Ghee, T.A., "Parametric Evaluation of Deployable Serrated Flaps on a Representative UCAV Configuration." AIAA-2003-3928

2. Ghee, T.A., "A Deployable Serrated Flap for Air Vehicle Control of a Representative UCAV Configuration" AIAA-2002-3276.

3. Ghee, T.A. and Doug R. Hill, "Experimental and Numerical Investigation of Vortex Shedding of a Representative UCAV Configuration for Vortex Flow Control" MP-69-P-34. Proceedings of the NATO Applied Vehicle Technology Panel (AVT) Symposium on Advanced Flow Management Part A – Vortex flows and High Angle of Attack, Leon, Norway, May 2001.

4. Bruce, R. J., Low Speed Wind Tunnel Tests on the UCAV concept, Unclassified QinetiQ Report, QINETIQ/FST/TR025502/1.0; March 2003.

5. Anderson, John D., "Fundamentals of Aerodynamics", 2nd ed., McGraw Hill Publishing Company, 1991.

6. Le Moigne, T, Rizzi, A. and Johansson, P., "CFD Simulations of a Delta Wing in High-Alpha Pitch Oscillations", AIAA Paper 01-0862 presented at the 39th Aerospace Sciences Meeting and Exhibit, 8-11 January 2001, Reno, NV.

7. Frink, N. T., "Recent Progress Toward a Three-Dimensional Unstructured Navier-Stokes Flow Solver", AIAA 94-0061, January 1994.

8. Pirzadeh, S., "Structured Background Grids for Generation of Unstructured Grids by Advancing Front Method", AIAA Journal, Vol. 31, No. 2, February 1993, pp. 257-265.

9. Pirzadeh, S., "Recent Progress in Unstructured Grid Generation ", AIAA Paper 92-0445, January 1992.

10. Anderson, W. K., and Bonhaus, D. L.: "An implicit Upwind Algorithm for Computing Turbulent Flows on Unstructured Grids", Computers Fluids, Vol. 23, No. 1, pp. 1-21, 1994.

11. Anderson, W. K.: "Grid Generation and Flow Solution Method for Euler Equations on Unstructured Grids", NASA TM.4295, April 1992.

12. W. K., Rausch, R.D., and Bonhaus, D. L.: "Implicit/Multigrid Algorithms for Incompressible Turbulent Flows on Unstructured Grids", J. Comp. Phys. Vol. 128, 1996, pp. 391-408.

13. Frink, N. T., "Upwind Scheme for Solving the Euler Equations on Unstructured Tetrahedral Meshes." AAA Journal, Vol., No. 1, January, 1992, pp. 70-77.

14. Parikh, P., Pirzadeh, S., and L R.., "A Package for 3-D Unstructured Grid Generation, Finite-Element Flow Solutions, and Flow-Field Visualization", NASA CR-182090, September 1990.

15. Frink, N. T., Pirzadeh, S., and Parikh, P., "An Unstructured-Grid Software System for Solving Complex Aerodynamic Problems", NASA CP-3291, pp. 289-308, May 9-11, 1995.

16. Frink, N. T., 'Assessment of an Unstructured-Grid Method for Predicting 3-D Turbulent Viscous Flows', AIAA 96-0292, January 1996.

17. Spalart, P. R. and Allmaras, S. R., "A One-Equation Turbulence Model for Aerodynamic Flows", AIAA Paper 92- 0439, January 1992.

18. Van Leer, B.: "Flux-Vector Splitting for the Euler Equations", Eighth International Conference on Numerical Methods in Fluid Dynamics, E. Krause, ed., Volume 170 of Lecture Notes in Physics, Springer-Verlag, 1982, pp. 507-512.